

See discussions, stats, and author profiles for this publication at: <https://www.researchgate.net/publication/339201604>

Doppler-Resilient 802.11ad-Based Ultra-Short Range Automotive Radar

Thesis · July 2019

CITATIONS

10

READS

14

3 authors, including:



Gaurav Duggal

Indraprastha Institute of Information Technology

5 PUBLICATIONS 18 CITATIONS

[SEE PROFILE](#)



Shobha Sundar Ram

Indraprastha Institute of Information Technology

43 PUBLICATIONS 587 CITATIONS

[SEE PROFILE](#)

Some of the authors of this publication are also working on these related projects:



On-Chip Wireless Channel Modelling [View project](#)



Automotive Radar [View project](#)

Doppler-Resilient 802.11ad-Based Ultra-Short Range Automotive Radar

A THESIS

SUBMITTED IN PARTIAL FULFILLMENT OF THE REQUIREMENTS FOR

THE DEGREE OF

M.Tech

By

Gaurav Duggal



Electronics and Communication Engineering

INDRAPRASTHA INSTITUTE OF INFORMATION TECHNOLOGY DELHI
NEW DELHI- 110020

June 2019

Acknowledgement

I would like to express my gratitude to my supervisor Dr. Shobha Sunder Ram who has been there for me as a technical advisor and personal guide. She has emphasized scientific rigor, both professional and personal integrity and forced me to go out of my comfort zones to explore the unknown. I dedicate this work to her.

I would like to thank Dr. Kumar Vijay Mishra for being a technical advisor to this work, Shelly Vishwakarma for being there to discuss new ideas and all the other inputs. I would also like to thank my peers Fatima and Dada who were there with me as a support throughout this work. Lastly I would like to thank my family and friends without whose constant support this work would not have been possible.

Certificate

This is to certify that the thesis titled "Doppler-Resilient 802.11ad-Based Ultra-Short Range Automotive Radar" being submitted by Gaurav Duggal (Roll No.- MT17091) to the Indraprastha Institute of Information Technology Delhi, for the award of the Master of Technology, is an original work carried out by him under my supervision. In my opinion, thesis has reached the standards fulfilling the requirements of the regulations relating to the degree. The results contained in the thesis have not been submitted in part or full to any other university or institute for the award of any degree/diploma.

Date: _____

Dr. Shobha Sundar Ram
Assistant Professor
Department of Electronics and Communication Engineering
Indraprastha Institute of Information Technology, Delhi
New Delhi 110020

Abstract

The IEEE 802.11ad link, identified as a key building block towards fifth-generation (5G) networks, has recently emerged as a candidate waveform for automotive radars. Prior works on such a system exploit the perfect autocorrelation property of the complementary Golay sequences embedded in the 802.11ad preamble for target detection. However, these studies either assume simple point scatterer representation for the automotive targets, apply 802.11ad for long ranges by ignoring severe signal attenuation at its 60 GHz carrier, or perform poorly for moving targets due to large range sidelobes of Golay pairs at non-zero Doppler shifts. Here, we address these issues by proposing 802.11ad for ultra-short range (less than 40 m) applications such as parking and lane change assistance; modeling automotive targets like pedestrians, bicycles, and cars as extended scatterers; and embedding the 802.11ad packets with the Doppler-resilient waveforms based on the Prouhet-Thue-Morse sequence. We realistically validate our methods for animated targets by simulating their scattering center models and, using the new waveform, obtain detailed signatures that exhibit micro-Doppler and high range resolution features. Our numerical experiments for objects such as a pedestrian, bicycle and car show very detailed features with at least 20 dB improvement in sidelobe levels for a Doppler-tolerant link when compared with a standard 802.11ad protocol. Further experiments show that our approach results in 2.5% reduction in probability of false alarm at low signal-to-noise-ratios and sidelobe suppression of 20 dB up to Doppler velocities of ± 144 km/h.

Contents

Certificate	i
Abstract	ii
List of Figures	v
List of Tables	vii
1 Introduction	1
1.1 Introduction	1
1.2 Motivation	1
1.3 Thesis Outline	5
2 Signal Model	6
2.1 Signal Model	6
2.1.1 Classical 802.11ad-based target localization	6
2.1.2 Doppler-resilient 802.11ad	9
3 Measurement Data	13
4 Target Models	17
4.1 Target Models	17
4.1.1 Animation model of car and bicycle	18
4.1.2 Animation model of pedestrians	18
4.1.3 Electromagnetic model of extended targets	19
5 Results	21
5.1 Experiments	21
5.1.1 Car	21
5.1.2 Bicycle	23
5.1.3 Pedestrian	24
5.1.4 Detection performance	24
6 Conclusion	27

6.1 Conclusion 27

Bibliography **28**

List of Figures

1.1	Simplified illustration of an automotive radar scenario. The white car on left is mounted with the radar whose approximate coverage is indicated by the gray triangular area. The solid white lines within this area indicate azimuth bins. The targets at close range (blue and orange pedestrians; blue and yellow cars) occupy several cross-azimuth bins. Such targets are modeled as multiple point scatterers, each of which exhibits micro-motion. On the contrary, the targets at long range (green and yellow pedestrians; green and orange cars) fill up only a part of a single azimuthal bin and their micro-motions are indistinguishable.	3
1.2	Structure of the SCPHY IEEE 802.11ad frame which consists of the preamble (CEF and STF), a header, data blocks (BLK) and optional training fields (omitted). The CEF contains G_{u512} , G_{v512} each of which comprises of a 256 length Golay complementary pair. The numbers in parenthesis represent the length of the sequence.	3
2.1	Proposed Doppler-resilient Golay sequence in the CEF across multiple packets in a coherent processing interval. Consecutive packets contain one member of the Golay pair in the CEF field G_{u512} that is 512-bit with time interval $T_{\text{fast}} = 0.5$ ns. A total of 2048 packets are transmitted.	7
2.2	Ambiguity function for a point scatterer at range 20 m and moving at 10 m/s using (a) standard Golay (SG) (b) Doppler Resilient Golay waveform.	10
3.1	Monostatic radar configuration using vector network analyzer in narrowband mode and two horn antennas.	14
3.2	Trajectories followed by (a) pedestrian, (b) bicycle and (c) car during measurement data collection. Micro-Doppler spectrograms of (d) pedestrian, (e) bicycle and (f) car obtained by performing STFT on 7.5 GHz narrowband measurement data.	15
3.3	Velocity of point scatterers distributed along a rotating wheel	15
4.1	Scattering center model of (a) a car, (b) a cycle and (c) a pedestrian. The trajectories traversed by all targets before the radar (red dot) are plotted in (d), (e) and (f) respectively.	17
5.1	(a) Trajectory of a car before the radar (b) Range-time plot of point scatterers on the car, (c) Radial velocity versus time of point scatterers on the car. Radar signatures: (d) SG range-time (e) MG range-time (f) SG Doppler-time (g) MG Doppler-time	22

5.2	(a) Range-time plot of the point scatterers on the bicycle, Radar Signatures: (b) SG range-time, (c) MG range-time (e) Doppler-time plot of the point scatterers on the bicycle, Radar Signatures: (f) SG Doppler-time (g) MG Doppler-time	22
5.3	(a) Range-time plot of point scatterers on the pedestrian, (d) Radial velocity versus time of point scatterers on the pedestrian. Radar signatures: (b) SG range-time (c) MG range-time (e) SG Doppler-time (f) MG Doppler-time	23
5.4	Histogram of car, pedestrian and noise signals for standard and modified Golay (a) at SNR of +5dB and (c) at SNR of -20dB. The P_d for SG and MG for different threshold values. The P_{fa} for SG and MG as a function of SNR of radar receiver.	23

List of Tables

3.1	Proposed radar parameters	14
-----	-------------------------------------	----

Chapter 1

Introduction

1.1 Introduction

During past few years, autonomous vehicles or self-driving cars have witnessed enormous development in vehicular control [1], environmental sensing [2], in-vehicle entertainment [3], efficient resource utilization [4], and inter-vehicular synchronization [5]. An ongoing challenge is automotive target detection and recognition in order to avoid road accidents and boost automotive safety. Conventional target detection techniques use sensors such as lidar [6], camera [7] and infrared/thermal detectors [8]. However, only radar offers the advantage of robust detection in adverse vision and weather conditions [2]. Currently, millimeter-wave (mmWave) automotive radars operating at 77 GHz are the preferred radar technology for target detection because they are characterized by wide bandwidths (~4-7 GHz) and, hence, very high range resolution [9–11].

1.2 Motivation

A concurrent development in intelligent transportation systems is the evolution of various vehicle-to-X (V2X) communication frameworks including vehicle-to-vehicle (V2V), vehicle-to-infrastructure (V2I), and vehicle-to-pedestrian (V2P) paradigms [12]. The overarching objective of these frameworks is to encourage sharing of road and vehicle information for applications such as environmental sensing, collision avoidance, and pedestrian detection. In the mmWave band, the IEEE

802.11ad protocol at unlicensed 60 GHz has been identified as a potential candidate for these communications because of high throughput advantages arising from wide bandwidth [9].

More recently, there is active research thrust towards combining automotive radar and communication functionalities on a single carrier 802.11ad wireless framework; the primary benefits being sharing of the common spectrum and hardware resources by the two systems (as already demonstrated at other bands [9, 13, 14]). The 802.11ad-based V2V joint radar-communications (JRC) was proposed in [15, 16]. The corresponding V2I application has been explored recently in [17] for radar-aided beam alignment to improve mmWave V2I communications. These works exploit the 802.11ad link to estimate ranges and Doppler velocities of automotive targets that are modeled as simple *point* scatterers. This representation based on Swerling-0 model [18] is appropriate for medium and long-range automotive radar applications where the far-field condition between the sensor and the target is sufficiently satisfied. In practice, however, 802.11ad is unsuitable for longer ranges because significant signal attenuation at 60 GHz arising from oxygen absorption severely restricts the maximum detectable radar range [18]. Therefore, it is more useful to employ 802.11ad-based JRC for *ultra-short* range radars (USRRs). These sensors operate below 40 m range and have garnered much interest for applications such as blind spot warning, closing vehicle detection, lane change assistance, park distance control, parking lot measurement and automatic park assistance [19].

Employing 802.11ad for USRRs leads to a second problem. When the target is located within a close range of a high-resolution radar, the received signal is composed of multiple reflections from different parts of the same object [13] (Fig. 1.1). When the automotive target moves, these point scatterers may often exhibit *micro-motions* besides the gross translational motion of the dynamic body. Examples include the swinging motion of the human arms and legs and the rotation of the wheels of a car. These micro-motions give rise to *micro-Doppler* features captured in joint time-frequency transforms [20, 21] and/or *micro-range* features captured in high range-resolution profiles [22]. These signatures are usually both distinctive and informative and have been used for target classification especially in the case of pedestrians [23]. This *extended* automotive target model is more general. But previous works on 802.11ad JRC represent targets as only point scatterers because, as we explain next, conventional 802.11ad waveform performs poorly in detecting both bulk and micro-motions.

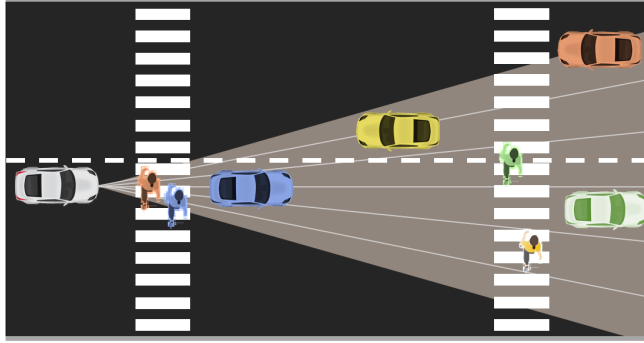


FIGURE 1.1: Simplified illustration of an automotive radar scenario. The white car on left is mounted with the radar whose approximate coverage is indicated by the gray triangular area. The solid white lines within this area indicate azimuth bins. The targets at close range (blue and orange pedestrians; blue and yellow cars) occupy several cross-azimuth bins. Such targets are modeled as multiple point scatterers, each of which exhibits micro-motion. On the contrary, the targets at long range (green and yellow pedestrians; green and orange cars) fill up only a part of a single azimuthal bin and their micro-motions are indistinguishable.

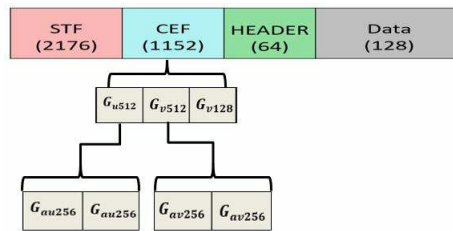


FIGURE 1.2: Structure of the SCPHY IEEE 802.11ad frame which consists of the preamble (CEF and STF), a header, data blocks (BLK) and optional training fields (omitted). The CEF contains G_{u512} , G_{v512} each of which comprises of a 256 length Golay complementary pair. The numbers in parenthesis represent the length of the sequence.

The physical layer of IEEE 802.11ad protocol transmits control (CPHY), single carrier (SC) and orthogonal frequency-division multiplexing (OFDM) modulation frames at chip rates of 1.76 GHz and 2.64 GHz, respectively. Every single CPHY and SCPHY frame is embedded with a 2172-bit short training field (STF), a 1152-bit channel estimation field (CEF), 64-bit header, data block and a beamforming training field (omitted, for simplicity, in Fig. 1.2). The CEF consists of two 512-point sequences $G_{u512}[n]$ and $G_{v512}[n]$ which encapsulate *Golay complementary pairs* [9]. These paired sequences have the property of perfect *aperiodic* autocorrelation which is beneficial for communication channel estimation [24] and radar remote sensing [15].

The 802.11ad-based radars proposed in [15–17] harness the zero sidelobe attribute of 802.11ad Golay pairs during the matched filtering stage of the radar receiver to estimate the target's location in a delay-Doppler plane [25, 26]. However, the perfect

auto-correlation property of Golay pairs holds strictly for only static targets. When the target is moving, the Doppler phase shift in the received signal causes a deterioration in the pulse compression output leading to large non-zero side lobes [27]. This effect is accentuated for multiple moving point targets as well as a single extended target with multiple point scatterers moving at different velocities. A large body of literature exists on designing single polyphase sequences [28] as well as generalizations of complementary Golay waveforms [29] to exhibit Doppler tolerance. In particular, [27] employed Prouhet-Thue-Morse sequence [30] to design Doppler-resilient Golay complementary pairs which are free of range sidelobes at modest Doppler shifts. Such a sequence is appropriate for detection of micro-motion signatures. In this work, we utilize the Gu_{512} field to construct Doppler-resilient Golay complementary sequences across multiple 802.11ad packets and show that their performance in detecting the micro-Doppler and micro-range signatures of extended automotive scatterers supersedes that of the standard 802.11ad waveform. We presented preliminary results with simplistic target models with non-fluctuating radar cross-section along constant velocity straight line trajectories in [31]. In this work, we present realistic simulation models of automotive targets accounting for size, shape, material and aspect properties along more complex trajectories involving acceleration from start, driving turns and returning to halt.

Specifically, we consider the following common targets: a small car which we model as a cluster of triangular plates with point scatterers on its body and four wheels, a bicycle that we model with cylinders and a pedestrian that we represent with ellipsoidal body parts and corresponding point scatterers. In each case, we consider target movement along a complex trajectory within the maximum unambiguous range of the radar. We then retrieve the high range resolution profiles and the Doppler spectrograms from these targets using the *standard* and the *modified* Doppler resilient Golay waveforms. Our results with the modified protocol show an improvement of approximately 20 dB in the range side-lobe suppression over the standard protocol. Interestingly, these side-lobe levels are retained up to Doppler velocities of ± 144 km/hr which is well beyond the maximum target speed for urban highways. We study the impact of the range sidelobe suppression on the radar detection performance in terms of the probability of detections (P_d) and false alarms (P_{fa}) for the standard and the modified Golay waveforms. We observe nearly identical values of P_d but a significant reduction in the P_{fa} - while using the modified Doppler resilient waveform - for low to moderate signal to noise ratios.

1.3 Thesis Outline

This thesis is divided into 6 chapters and an overview of each chapter is given below:

- **Chapter 2: Signal Model**

In this chapter we describe the signal model of 802.11ad-based radar and introduce our proposed Doppler-resilient link.

- **Chapter 3: Measurement Data**

In this chapter we present Doppler radar signatures of common automotive targets at short ranges as measured by an actual radar

- **Chapter 4: Target Models**

In this chapter we present the models of three automotive targets for the 802.11ad-based radar.

- **Chapter 5: Experiments**

In this chapter we validate our methods through numerical experiments and study the detection performance of the radar.

- **Chapter 6: Conclusion**

This chapter concludes all the findings of this work.

Chapter 2

Signal Model

2.1 Signal Model

The range and Doppler estimation methods using the SCPHY CEF field of standard 802.11ad are described in [15, 17, 24]. In [16], estimation of target parameters using the CPHY frame has been mentioned. In the following, we introduce the radar signal model based on 802.11ad SCPHY that we have adapted for extended targets.

2.1.1 Classical 802.11ad-based target localization

A *Golay complementary pair* consists of two unimodular sequences $G_{1,N}$ and $G_{2,N}$ both of the same length N such that the sum of their autocorrelations has a peak of $2N$ and a side-lobe level of zero:

$$G_{1,N}[n] * G_{1,N}[-n] + G_{2,N}[n] * G_{2,N}[-n] = 2N\delta[n]. \quad (2.1)$$

In previous studies [15–17, 24, 31], the Golay complementary pair members $G_{a_{256}}$ and $G_{b_{256}}$ are drawn from the CEF of the same packet (Fig. 1.2). When these pairs are correlated at the receiver, the pulse repetition intervals (PRIs) for both sequences in the pair differ by a delay equivalent to the transmission time of one 256-bit sequence. Such a non-uniform PRI has a bearing on Doppler estimation but was ignored in the previous studies that investigated only macro-Doppler features. In this work, to keep the PRI same among all members of the Golay pair, we propose that the complementary

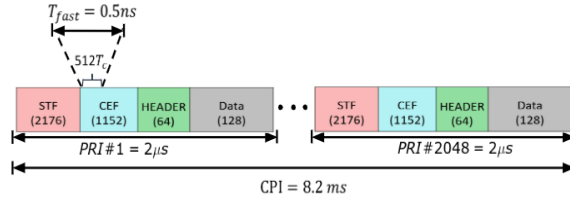


FIGURE 2.1: Proposed Doppler-resilient Golay sequence in the CEF across multiple packets in a coherent processing interval. Consecutive packets contain one member of the Golay pair in the CEF field $G_{u_{512}}$ that is 512-bit with time interval $T_{\text{fast}} = 0.5$ ns. A total of 2048 packets are transmitted.

sequences are of length 512 and embedded in the $G_{u_{512}}$ of CEF alternately in two consecutive packets as shown in Fig. 2.1. For the p th packet, the transmit signal is the 512-bit Golay sequence in CEF:

$$s_T[n] = G_{p,512}[n], \quad n = 0, 1, \dots, 511, \quad (2.2)$$

where $G_{p,512}$ and $G_{(p+1),512}$ are Golay complementary pairs. The discrete-time sequence $s_T[n]$ is passed through a digital-to-analog-converter (DAC) the output of which can be represented as a weighted sum of Dirac impulses:

$$s_T(t) = \sum_{n=0}^{511} s_T[n] \delta(t - nT_c), \quad (2.3)$$

where $F_c = 1.76$ GHz $= 1/T_c$. This signal is then amplified to impart energy E_s per symbol to the transmit signal. The amplifier output is passed through a transmit shaping filter $h_T(t)$ to obtain

$$x_T(t) = \sqrt{E_s} (s_T * h_T)(t) = \sum_{n=0}^{511} s_T[n] h_T(t - nT_c). \quad (2.4)$$

The 802.11ad protocol specifies a spectral mask for the transmit signal to limit inter-symbol interference (ISI) [32, section 21.3.2]. We assume that $h_T(t)$ includes a low-pass baseband filter with an equivalent amplitude characteristic of the spectral mask. A common shaping filter has a frequency response $H_T(f)$ of the root raised cosine (RRC) filter [33]. At the receiver, another RRC filter $h_R(t)$ is employed such that the net frequency response is equal to a raised cosine (RC) filter, $H(f) = H_T(f)H_R(f)$. The RC filter is a Nyquist filter with the following time-domain property to avoid ISI:

$$h[n] = h(nT_c) = \begin{cases} 1, & n = 0 \\ 0, & n \neq 0 \end{cases}. \quad (2.5)$$

We can formulate this as:

$$h(t) = \sum_{k=-\infty}^{+\infty} \delta(t - kT_c) = \delta(t). \quad (2.6)$$

This property only holds for the RC, and not the RRC filter. The baseband signal is then upconverted for transmission: $x(t) = x_T(t)e^{j2\pi f_c t}$, where f_c denotes the carrier frequency. The duration of this transmitted signal is $512T_c = 0.5$ ns and the number of fast time samples is therefore 512. If we assume that the data block consists of 16 Bytes and that there are no optional training fields then each packet is of $T_p = 2$ μ s duration which corresponds to the pulse repetition interval.

Assume that the radar transmits P packets constituting one coherent processing interval (CPI) towards a direct-path extended target of B point scatterers, where a b th point is characterized by a time-varying complex reflectivity $a_b(t)$ located at range $r_b = c\tau_b/2$ and Doppler $f_{D_b} = \frac{2v_b}{\lambda}$, $c = 3 \times 10^8$ m/s is the speed of light, τ_b is the time delay, v_b is the associated radial velocity and λ is the radar's wavelength. The coefficient a_b subsumes common effects such as antenna directivity, processing gains and attenuations including path loss. Ignoring the multi-path components, the reflected received signal at the baseband, i.e., after down-conversion, is

$$\begin{aligned} x_R(t) &= \sum_{p=0}^{P-1} \sum_{b=1}^B a_b(t) x_T(t - \tau_b - pT_p) e^{-j2\pi f_{D_b} t} + z(t) \\ &\approx \sum_{p=0}^{P-1} \sum_{b=1}^B a_b(t) x_T(t - \tau_b - pT_p) e^{-j2\pi f_{D_b} pT_p} + z(t), \end{aligned} \quad (2.7)$$

where $z(t)$ is additive circular-symmetric white Gaussian noise. The last approximation follows from the fact that $f_{D_b} \ll 1/T_p$ so that the phase rotation within one coherent processing interval (CPI) (*slow time*) can be approximated as a constant. Sampling the signal at $F_c = 1/T_c$ yields $x_R[n] = x_R(nT_c)$:

$$\begin{aligned} x_R[n] &= \sum_{p=0}^{P-1} \sum_{b=1}^B a_b[n] x_T(nT_c - \tau_b - pT_p) e^{-j2\pi f_{D_b} pT_p} + z(nT_c) \\ &= \sum_{p=0}^{P-1} \sum_{b=1}^B a_b[n] s_T(nT_c - \tau_b - pT_p) e^{-j2\pi f_{D_b} pT_p} + z[n], \end{aligned} \quad (2.8)$$

where we used Nyquist filter properties (2.5-2.6) in the last equality.

When the sampled signal from two consecutive packets is passed through matched filters of each Golay sequence, we exploit the perfect autocorrelation property to estimate the radar channel. For instance, correlation for the p^{th} pair produces

$$\begin{aligned}\hat{h}_p[n] &= x_R[n] * G_{p,512}[-n] \\ \hat{h}_{p+1}[n] &= x_R[n] * G_{p+1,512}[-n]\end{aligned}\quad (2.9)$$

These outputs are added to return the channel estimate

$$\begin{aligned}\hat{h}[n] &= \frac{1}{1024}(\hat{h}_p[n] + \hat{h}_{p+1}[n]) \\ &\approx \frac{1}{1024} \sum_{p=1}^P \sum_{b=1}^B a_b[n] \delta(nT_c - \tau_b - pT_p) e^{-j2\pi f_{D_b} pT_p} \\ &\quad + z[n] * (G_{p,512}[-n] + G_{p+1,512}[-n]),\end{aligned}\quad (2.10)$$

where the last approximation is due to the assumption that the Doppler shifts are nearly identical for the two Golay sequences $G_{p,512}$ and $G_{p+1,512}$ to utilize the zero side-lobe property of (2.1). In order to locate the targets in the delay-Doppler plane, the range-time space is discretized into 512 bins of $cT_c/2$ resolution ($r = \frac{cT_c n}{2}, \{n = 0 : 511\}$). We then create a delay-Doppler map by taking a 512-point Discrete Fourier Transform (DFT) of the radar channel estimates for each Doppler shift bin. Then, the delay and Doppler frequencies of the point scatterers on the target are given by the location of the B peaks on this 2D delay-Doppler map. For each m^{th} CPI, the peaks along the Doppler axes for each range bin are coherently summed to obtain the time-varying high range resolution profile $\chi_{RT}[m, r]$. Similarly, the peaks along the range axes for each Doppler bin are coherently summed to obtain the Doppler (or velocity) - time spectrogram $\chi_{DT}[m, f_D]$.

2.1.2 Doppler-resilient 802.11ad

When a target is moving, the Doppler based phase shifts across the two waveforms may differ. For example, a point scatterer moving with a Doppler shift of f_{D_b} will give rise to a phase shift of $\theta \approx 2\pi f_{D_b} T_p$ between \hat{h}_p and \hat{h}_{p+1} . In this case, the perfect autocorrelation would no longer hold, i.e.,

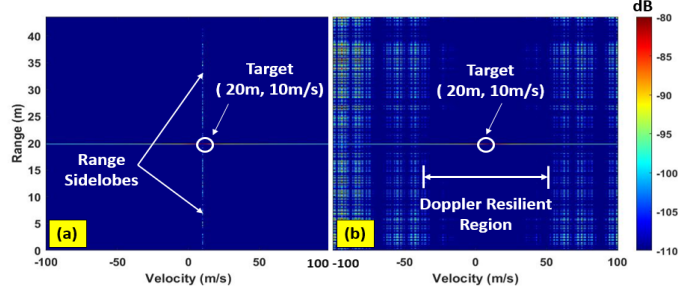


FIGURE 2.2: Ambiguity function for a point scatterer at range 20 m and moving at 10 m/s using (a) standard Golay (SG) (b) Doppler Resilient Golay waveform.

$$(G_{p,N}[n] * G_{p,N}[-n]) + (G_{p+1,N}[n] * G_{p+1,N}[-n]) e^{-j\theta} \neq 2N\delta[n], \quad (2.11)$$

resulting in high side-lobes along the range. For example, consider a simple nonfluctuating point scatterer of unit reflectivity at $(r_b = 20 \text{ m}, v_b = 10 \text{ m/s})$ over 1 CPI of $P = 2048$ packets. For this set of waveform parameters, Fig. 2.2a plots the *range-Doppler ambiguity function* (AF) obtained by correlating the waveform with its Doppler-shifted and delayed replicas. The AF completely characterizes the radar's ability to discriminate in both range and velocity of its transmit waveform. The complementary Golay AF shows a very high sidelobe level of -20 dB at non-zero Doppler frequencies. This would result in *high false alarms* especially at low signal to noise ratios (SNR).

The limitation described above can be overcome by using Doppler-tolerant Golay sequences such as the one proposed in [27]. Without loss of generality, assume P be even and generate the Prouhet-Thue-Morse (PTM) sequence [30], $\{q_p\}_{p=0}^{\frac{P}{2}-1}$ which takes values in the set $\{0, 1\}$ by following Boolean recursion:

$$q_p = \begin{cases} 0, & \text{if } p = 0 \\ q_{\frac{p}{2}}, & \text{if } (p \text{ modulo } 2) = 0 \\ \overline{q_{\frac{p-1}{2}}}, & \text{if } (p \text{ modulo } 2) = 1, \end{cases} \quad (2.12)$$

where $\overline{q_p}$ denotes the binary complement of q_p . As an example, when $P = 16$, the PTM sequence is $q_0 = \{0, 1, 1, 0, 1, 0, 0, 1\}$.

Based on the values of q_p , we transmit the following Golay pairs: if $q_1 = 0$, then the complementary pair $G_{1,N}[n]$ and $G_{2,N}[n]$ are transmitted separately in two consecutive packets; if $q_2 = 1$, then the consecutive transmission consists of the complementary pair with $-G_{2,N}[-n]$ and $G_{1,N}[-n]$; and so on. In this manner, we transmit a sequence of Doppler-resilient Golay sequences over P packets. The goal is to obtain a pulse train

of Golay pairs such that

$$\sum_{p=0}^{P-1} e^{jn\theta} (G_{p,N}[n] * G_{p,N}[n]) \approx f(\theta)\delta[n], \quad (2.13)$$

where the function $f(\theta)$ does not depend on the time-shift index n for some reasonably large values of θ . The Taylor series approximation of the left-hand-side of (2.13) around zero Doppler is

$$\begin{aligned} \sum_{p=0}^{P-1} e^{jn\theta} (G_{p,N}[n] * G_{p,N}[n]) \approx \\ 0(G_{0,N}[n] * G_{0,N}[n]) + 1(G_{1,N}[n] * G_{1,N}[n]) + 2(G_{2,N}[n] * G_{2,N}[n]) + \dots \\ + (P-1)(G_{P-1,N}[n] * G_{P-1,N}[n]). \end{aligned} \quad (2.14)$$

Using PTM sequence, the above summation can be made to approach a delta function. The key is to transmit a Golay sequence that is also complementary with sequences in more than one packet. For instance, when $P = 4$, the PTM sequence dictates sending following signals in consecutive packets: $G_{1,N}[n]$, $G_{2,N}[n]$, $-G_{2,N}[-n]$ and $G_{1,N}[-n]$ for an arbitrary Golay pair $\{G_{1,N}[n], G_{2,N}[n]\}$. In such a transmission, not only the first and last two sequences are Golay pairs but also the second and fourth signals. This implies

$$\begin{aligned} \sum_{p=0}^3 e^{jn\theta} (G_{p,N}[n] * G_{p,N}[n]) &\approx 1(G_{1,N}[n] * G_{1,N}[n]) + 2(G_{2,N}[n] * G_{2,N}[n]) \\ &\quad + 3(G_{3,N}[n] * G_{3,N}[n]) \\ &= 1((G_{1,N}[n] * G_{1,N}[n]) + (G_{3,N}[n] * G_{3,N}[n])) + 2((G_{2,N}[n] * G_{2,N}[n]) \\ &\quad + (G_{3,N}[n] * G_{3,N}[n])) \\ &= (2N + 2(2N))\delta[n] \\ &= 6N\delta[n]. \end{aligned} \quad (2.15)$$

For these Doppler-resilient Golay sequences, the resultant AF plot is nearly free of range sidelobes especially at low Doppler velocities. For the same target and waveform parameters as in Fig. 2.2a, the corresponding AF plot for Doppler resilient

Golay sequences is shown in Fig. 2.2b. We note that the Doppler resilience holds for target velocities up to approximately ± 40 m/s ($= \pm 144$ km/hr) which is above most of the velocities encountered in automotive scenarios. Hence, this waveform is suitable for V2P and USRR applications. From here on, we refer to the Doppler resilient Golay sequences as modified Golay (MG) and the original sequences presented in (2.1) as standard Golay (SG).

The IEEE 802.11ad physical layer (PHY) transmits single carrier (SC) modulation frames at chip rates of 1.76 GHz at a carrier frequency of 60 GHz. The range resolution is 0.085 m, determined by the chip rate of 1.76 GHz and the maximum range is 44 m corresponding to 512 fast-time samples. In order to detect velocity accuracy of approximately 0.3 m/s, we require a Doppler resolution of 122 Hz and a CPI of 8.2 ms. This implies transmission of $P = 2048$ packets to form a single CPI. The maximum unambiguous velocity ν_{max} is determined by the PRI T_p : $\nu_{max} = \lambda/T_p$. Table 3.1 summarizes the parameters of the proposed waveform. Better Doppler resolutions are possible by increasing the packet length.

Chapter 3

Measurement Data

Unlike previous 802.11ad radar studies that assume only simple point targets at long ranges, real world automotive targets such as pedestrians, bicycles and cars appear as extended scatterers to the radar, more so at close ranges. We demonstrate this aspect with measured data in this section. We collected narrowband micro-Doppler data of a pedestrian, bicycle and a car using a monostatic radar consisting of a N9926A FieldFox vector network analyzer (VNA) and two horn antennas (HF907) (Fig. 3.1). The VNA was configured to carry out narrowband S_{21} parameter measurements at a carrier frequency of 7.5 GHz, with transmitted power set at 3 dBm and sampling frequency at 370 Hz (maximum frequency that can be obtained in the narrowband mode). The gain of both horn antennas is 10 dBi. The return echoes of targets were recorded separately.

The time-domain narrowband data, $x_R[n]$, are processed using discrete-time short-time Fourier transform (STFT) to obtain the Doppler-time spectrogram, $\chi_{DT}[m, f_D]$:

$$\chi_{DT}[m, f_D] = \sum_{n=-\infty}^{\infty} x_R[n]w[n-m]e^{-j2\pi n f_D T_{\text{short}}}, \quad (3.1)$$

where $w[n] = 0.54 - 0.48 \cos(2\pi n/N)$ is the Hamming window of duration $T_{\text{short}} = 0.05$ s ($N = 20$).

The trajectories of the three targets are shown in Fig. 3.2. First, we consider a pedestrian of height 1.73 m. The subject walks towards the radar from a distance of 8 m (Fig. 3.2a) with an approximate speed of 1 m/s. The resulting micro-Doppler spectrogram (Fig. 3.2d) demonstrates that the pedestrian must be regarded as an

TABLE 3.1: Proposed radar parameters

Parameter	Proposed V2P Radar
Carrier frequency (GHz)	60
Bandwidth (GHz)	1.76
Range resolution (m)	0.085
Maximum unambiguous range (m)	44
Pulse repetition interval (μ s)	2
Velocity resolution (m/s)	0.3
Maximum unambiguous velocity (m/s)	625



FIGURE 3.1: Monostatic radar configuration using vector network analyzer in narrowband mode and two horn antennas.

extended target because micro-Doppler features from the torso, arms and legs are clearly visible on the radar. all the micro-Dopplers are positive when the pedestrian is approaching the radar. The swinging motions of the legs give rise to the highest Dopplers, followed by the arms and the torso. Next, we consider a bicycle target of height 1.1 m, length 1.8 m and wheels of 0.45 m radius. The bicycle starts from a distance of 10m and then turns left 2 m before the radar (Fig.3.2b). The corresponding spectrogram (Fig.3.2e) indicates that when the bicycle is moving straight towards the radar, only the micro-Dopplers from its frame are visible. However, when it executes a turn before the radar, multiple Doppler components arise from this single target. Besides the translational motion of the bicycle, the rotational motion of the two wheels turning at different velocities with respect to the radar; the motion of the pedals, and the small adjustments of the handle bars required for maintaining the balance of the bicycle also produce micro-Dopplers. These features are best observed during 6-9 s. Finally, we consider a small size car (Hyundai Grand I10) of dimensions 3.765 m \times

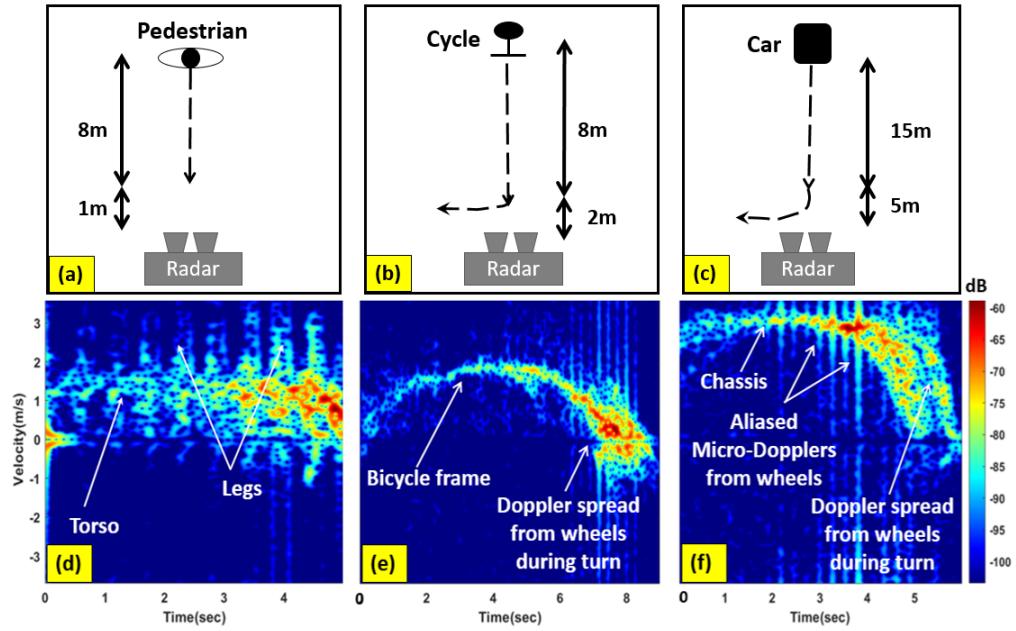


FIGURE 3.2: Trajectories followed by (a) pedestrian, (b) bicycle and (c) car during measurement data collection. Micro-Doppler spectrograms of (d) pedestrian, (e) bicycle and (f) car obtained by performing STFT on 7.5 GHz narrowband measurement data.

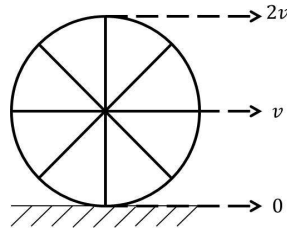


FIGURE 3.3: Velocity of point scatterers distributed along a rotating wheel

1.66 m \times 1.52 m and wheels of radius 0.36 m. The car moves from a distance of 20 m from the radar and then turns left before the radar at a distance of about 5 m (Fig. 3.2c). The chassis of the car moves with an average speed of 3 m/s which generates translational Doppler. But the rotational motion of the wheels introduce micro-Dopplers (Fig. 3.2f). Any point on the circumference of the wheel moves with a cycloidal motion. If the speed of the center of the wheel is v m/s, then the speed of the top of the wheel is $2v$ m/s while the speed of the base of the wheel is 0 m/s due to frictional forces as shown in Fig. 3.3. Therefore, the micro-Dopplers from the four wheels are spread from 0 to twice the mean Doppler from the chassis when the car moves in a straight line. Note that the angular velocities of the four wheels are usually identical in this scenario. However, depending on the path taken by the vehicle, the radial velocity components of the four wheels with respect to the radar may differ resulting in slightly varying micro-Doppler values. The returns from the wheels are

usually much weaker than the strong Doppler from the chassis and, hence, are visible only when the car is near the radar (Fig. 3.2c). Due to the limited sampling frequency of the radar receiver (370 Hz), some aliased micro-Doppler components from the rotation of the wheels at the lower frequencies also show up. When the car is turning before the radar, then the right and left wheels turn at different radii resulting in very different radial velocities. This results in a large micro-Doppler spread that appears during 4-6 s in the spectrogram.

The measurement results show that typical automotive targets are extended targets at short ranges, resulting in distinctive micro-Doppler spectrograms. They, therefore, engender similar micro-range features in high range resolution profiles generated with broadband radar data. In the following section, we discuss the modeling of these extended target models of pedestrians, bicycles and cars before applying our new Doppler-resilient waveform and its associated processing.

Chapter 4

Target Models

4.1 Target Models

There are multiple methods for generating animation models of dynamic bodies [34]. In this work, we derive the animation data of pedestrians from motion capture technology and use a physics based simulator to model the motion of a car and bicycle.

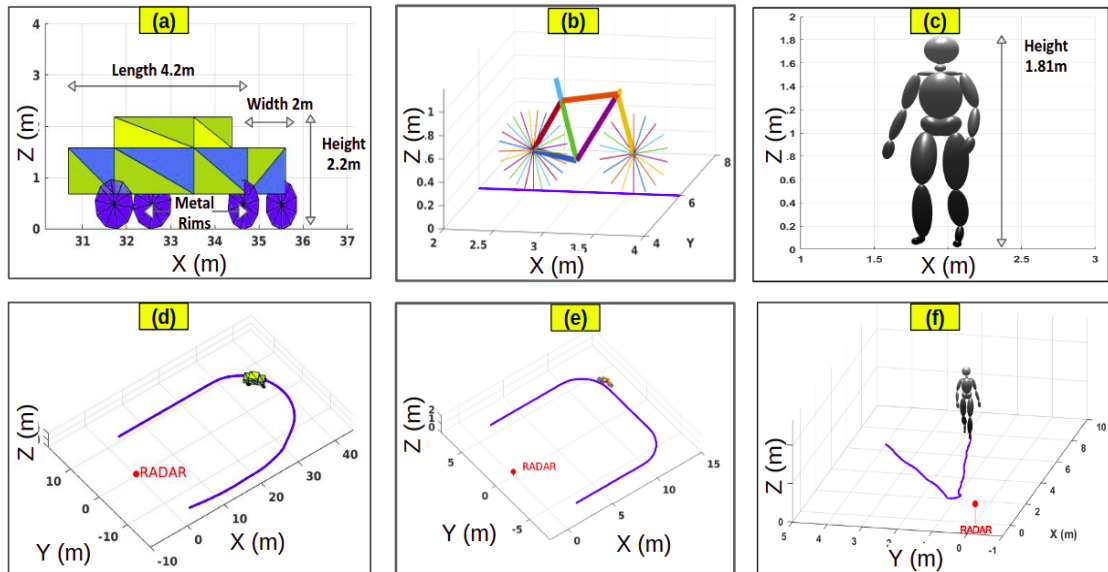


FIGURE 4.1: Scattering center model of (a) a car, (b) a cycle and (c) a pedestrian. The trajectories traversed by all targets before the radar (red dot) are plotted in (d), (e) and (f) respectively.

4.1.1 Animation model of car and bicycle

We employed pyBullet - a Python based open source software development kit (SDK) - for generating motion data of a car and bicycle [35]. PyBullet uses Bullet Physics, a physics-based animation package, for describing motions of dynamic bodies [36]. In this environment, each vehicle is designed as a collection of interconnected rigid bodies such that they do not undergo any type of physical deformation during motion. We modeled the car with a lateral wheel axle length of 2 m, front axle to rear axle length of 3.5 m and a wheel radius of 0.48 m as shown in Fig. 4.1a. We simulated *front wheel driving* of the car by considering the root of the compound body at the center of the axle connecting the two front wheels of the car. The root has six primary degrees of freedom (DOF) - translation along the three Cartesian axes and rotation around the same axes. A user *drives* the vehicle at the desired speed and along the desired trajectory by prescribing specific kinematic trajectories to the root. Secondary parts such as wheels are connected to the primary body through joints or hinges. The simulator then computed forces and torques that actuate the secondary DOFs of the joints to follow freely based on forward dynamics. The resulting motions of all the bodies comprising the vehicle are constrained by a control system in the software to realize realistic animation of the vehicle at a frame rate of 1000 Hz. With the radar at the origin, we considered a trajectory of the car as shown in Fig. 4.1d. The car accelerates from start, moves along a straight line to the left of the radar and then performs a U turn and moves towards the radar on a path to its right and then decelerates to a halt. The car is always within the maximum unambiguous range of the radar.

In the case of the bicycle, we consider a bicycle frame with a cross bar frame and two wheels as shown in Fig. 4.1b. For the sake of simplicity, we do not model the human rider on the bicycle. Through the PyBullet software, we obtain a realistic animation model of the two wheels, the bicycle frame and the front handle bars along the trajectory shown in Fig. 4.1e. The bicycle accelerates from halt and reaches a steady velocity and then performs two right turns before halting.

4.1.2 Animation model of pedestrians

The animation data of a walking human was obtained from motion capture technology at Sony Computer Entertainment America. The data describes the time-varying three-dimensional positions of a collection of markers distributed over the body of a

live actor at a frame rate of 60 Hz over a duration of 5 s. There are 24 markers located at the head, torso (both front and back), upper arms, hands, knees and feet. We assume that these markers correspond to the point scatterers on the body of the pedestrian as shown in Fig. 4.1c. The trajectory followed by the subject is shown in Fig. 4.1f. Here the pedestrian approaches the radar and then turns around and walks away from the radar.

4.1.3 Electromagnetic model of extended targets

We integrate the animation data of the pedestrian, bicycle and car with electromagnetic models of radar scattering using the primitive modeling technique [34] which has been extensively employed for modeling radar returns from dynamic human motions [37]. We first interpolate the animation data from the video frame rate to the radar sampling rate. Then, each of the dynamic bodies is modelled as an extended target made of multiple primitives with point scatterers distributed along its body. The car is assumed to be composed of 56 triangular plates. The wheel-rims and car body have been modeled as metallic plates. The windows, front windscreen and rear windscreen screen are modelled as glass. The radar cross section of each b^{th} plate at each n^{th} discrete time instance is :

$$\sigma_b[n] = \frac{4\pi A_b^2 \cos^2 \theta_b[n]}{\lambda^2} \left(\frac{\sin \left(kd_b \sin \frac{\theta_b[n]}{2} \right)}{kd_b \sin \frac{\theta_b[n]}{2}} \right)^4, \quad (4.1)$$

where A_b is the area of the triangle, d_b is the dimension of the triangle along aspect angle and $k = \frac{2\pi}{\lambda}$ is the phase constant for λ wavelength [38]. The aspect angle $\theta_b[n]$ is defined as the angle between the incident ray from the radar and the normal to the triangular plate.

In the case of the bicycle, we have modelled the Argon 18 Gallium bicycle. The bicycle frame consists of 9 metal cylinders of 6cm radius of differing lengths. The front wheel has 18 spokes and the rear wheel has 25 spokes, each of which are of 2mm radius and 34.5 cm length. The radar cross-section of a cylinder [38] of length L_b and radius a_b is:

$$\sigma_b[n] = \frac{2\pi a_b L_b^2}{\lambda} \cos^2(\theta_b[n]) \left(\frac{\sin(kL_b \sin \theta_b[n])}{kL_b \sin \theta_b[n]} \right)^2, \quad (4.2)$$

For the pedestrian, 21 different body parts - torso, arms and legs - are modelled as ellipsoids while the head is approximated as a sphere. The longest dimension of each ellipsoid spans the length of the bone in the skeleton structure of the motion capture

data. The radar cross section of an ellipsoid [38] of length H_b and radius R_b is

$$\sigma_b[n] = \frac{\frac{1}{4}R_b^4 H_b^2}{R_b^2 \sin^2 \theta_b[n] + \frac{1}{4}H_b^2 \cos^2 \theta_b[n]}. \quad (4.3)$$

The radar cross-section fluctuates with time due to the variation in angle $\theta_b[n]$ between incident wave and the major length axis of ellipsoid. We assume that the ellipsoids are made of single layer dielectric with a of dielectric constant 80 and conductivity 2.

If we assume that the transmitted power and antenna processing gains of the transmitter and receiver antennas is unity, then the strength of the scattered signal from the b^{th} part of the extended target depends on the material properties, aspect angle and the position of the scattering center on the primitive with respect to the radar. We incorporate the material properties of the target into the RCS estimation through Fresnel reflection coefficient, Γ , for planar interfaces at normal incidence. The attenuation of 60GHz wave through the air medium is modeled through α . Since all the scattering centers may not be visible to the radar at each time instant due to shadowing by other parts of the same target or other channel conditions, we incorporate stochasticity in the scattering center model by including a Bernoulli random variable of mean 0.5, i.e. $\zeta_b[n] \sim \text{Bernoulli}(0.5)$, in the RCS. A point scatterer is *seen* by the radar with a probability of 50% at every time instant. The reflectivity of a primitive at any time sample is

$$a_b[n] = \zeta_b[n] \Gamma(\theta_b[n]) \sqrt{\sigma_b[n]} \frac{e^{-j2\frac{2\pi}{\lambda}r_b[n] - 2\alpha r_b[n]}}{r_b^2[n]}. \quad (4.4)$$

The received signal, $x_R[n]$, is obtained from the sum of the convolution of the scattered signal from each b^{th} part and the transmitted signal as shown in (2.8). The noise is modeled as an additive zero-mean Gaussian noise with variance N_p . The primitive-based technique, presented here, is computationally efficient and relatively accurate in generating micro-Doppler signatures and high range resolution profiles. However the method does not capture the multipath effects.

Chapter 5

Results

5.1 Experiments

We evaluated our proposed approach through numerical experiments for common automotive targets such as a car, bicycle and a pedestrian. We compared the results for both SG and MG waveforms. The noise variance in all experiments is -100 dBm.

5.1.1 Car

Figure 5.1a shows the ground truth of the range-time for different point scatterers situated on the moving car. The range increases as the car moves away from the radar and then make a U turn at $t = 8$ s after which the range again begins to reduce. The range-time plots for SG and MG in Fig. 5.1b and c, show very good agreement with the ground truth range-time plot. In the inset, we observe the micro-range features that arise from the different point scatterers on the car. Due to the effect of shadowing, the range tracks show some discontinuities. The range resolution of the radar is sufficient at some time instances in resolving these micro-range tracks. The SG signature shows significant range sidelobes due to the motion of the car. These sidelobes are absent in the case of the MG signatures.

Figure 5.1d shows the ground truth of the velocity time behaviour of the point scatterers. The velocity-time results (Fig. 5.1e and f) show that there is considerable variation in the velocities of the different point scatterers on the body of the car and especially from the wheel. The velocities of different points on the chassis of the car also show variation

depending on their proximity and aspect with respect to the radar. The velocity-time radar signatures for both standard and modified Golay agree with the ground truth velocity-time plots. The micro-Doppler tracks of the different point scatterers can be easily observed. Results for SG and MG are nearly identical. This is because the motion of the car only affects the range dimension and not the Doppler dimension.

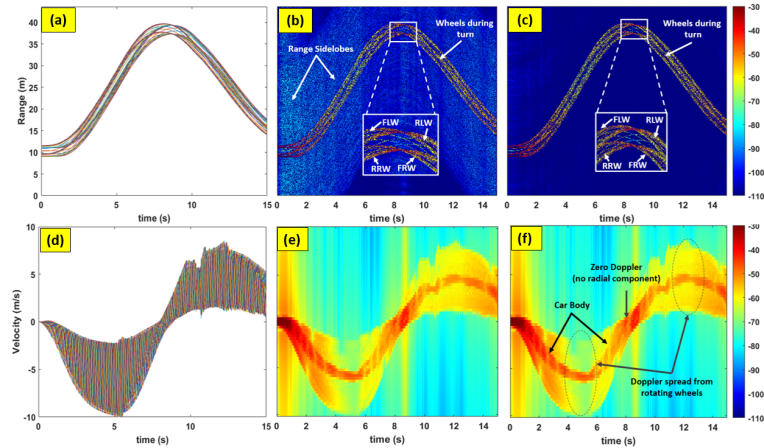


FIGURE 5.1: (a) Trajectory of a car before the radar (b) Range-time plot of point scatterers on the car, (c) Radial velocity versus time of point scatterers on the car. Radar signatures: (d) SG range-time (e) MG range-time (f) SG Doppler-time (g) MG Doppler-time

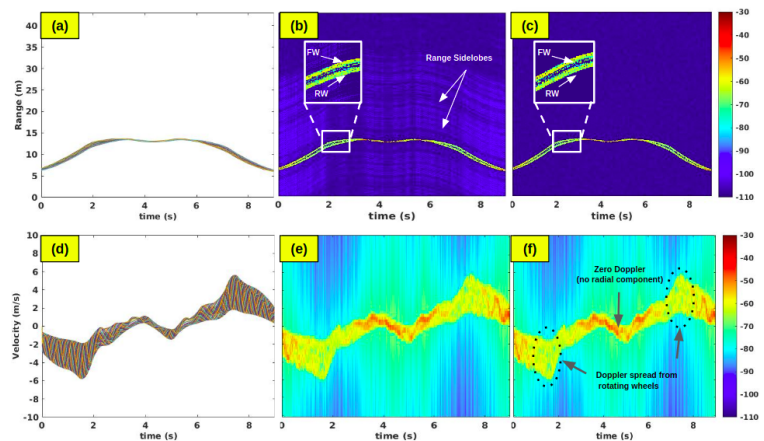


FIGURE 5.2: (a) Range-time plot of the point scatterers on the bicycle, Radar Signatures: (b) SG range-time, (c) MG range-time (e) Doppler-time plot of the point scatterers on the bicycle, Radar Signatures: (f) SG Doppler-time (g) MG Doppler-time

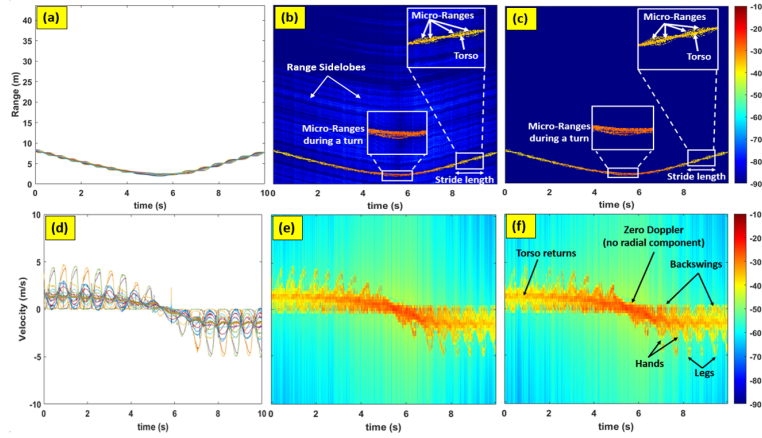


FIGURE 5.3: (a) Range-time plot of point scatterers on the pedestrian, (d) Radial velocity versus time of point scatterers on the pedestrian. Radar signatures: (b) SG range-time (c) MG range-time (e) SG Doppler-time (f) MG Doppler-time

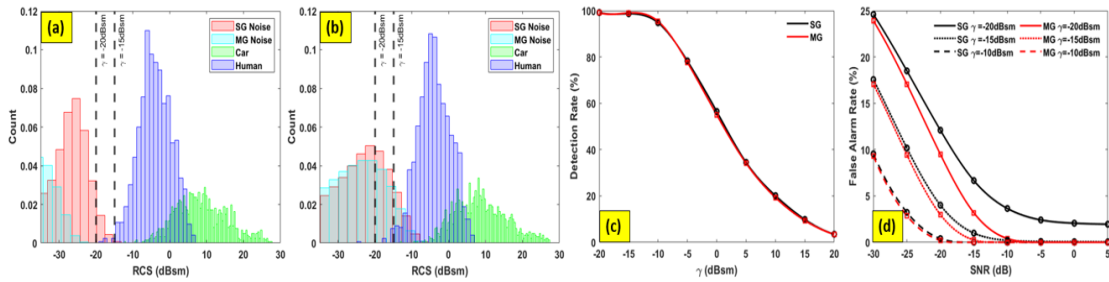


FIGURE 5.4: Histogram of car, pedestrian and noise signals for standard and modified Golay (a) at SNR of +5dB and (c) at SNR of -20dB. The P_d for SG and MG for different threshold values. The P_{fa} for SG and MG as a function of SNR of radar receiver.

5.1.2 Bicycle

The micro-range and micro-Doppler features from the motion of the bicycle are presented in Fig.5.2. The ground truth range-time plots of the different point scatterers on the two wheels show a very narrow range spread except during the turns (at 1.5s and 7s) - especially in comparison to the car. The high range resolution profiles for SG and MG waveforms are very similar to the ground truth plots. However, the high range sidelobes are evident in the SG plots. The velocity-time plots show a significantly greater Doppler spread due to the rotating wheels. The spread is greatest during turns which is similar to the results from the experimental measurements. The results from SG and MG look nearly identical here and are very similar to the ground truth results.

5.1.3 Pedestrian

Next, we study the radar signatures of the pedestrian in Fig. 5.3. We observe again that the range-time plots for SG (Fig. 5.3b) and MG (Fig. 5.3c) sequences are in agreement with the ground truth results (Fig. 5.3a). Due to the smaller spatial extent of the pedestrian across the range dimension, the micro-range tracks are difficult to observe except at some time instants. The inset shows the micro-range from the right and left legs and arms. The pedestrian is always within the maximum unambiguous range and the field of view of the radar. The radar cross-section of the pedestrian is typically lower than that of the car. However, since the pedestrian's trajectory is within 2m to 8m while the car moved from 10m to 40m, the signal strengths from both the cases are comparable. Again, we observe that the range-time plots of the SG sequence have high sidelobes levels when compared to the peak signal strength. These sidelobes are suppressed with the MG sequence. The Doppler velocity-time spectrograms in Fig. 5.3(d)-(f) show excellent agreement with the ground truth results. We observe the micro-Dopplers from the feet, legs, arms and torso. The Dopplers are positive when the pedestrian approaches the radar and are negative when the pedestrian moves away from the radar. The strongest Dopplers arise from the torso. As observed before in the results with the car, the signatures from the standard and modified Golay are nearly identical in the Doppler domain.

5.1.4 Detection performance

We now examine the impact of range sidelobes on the radar detection performance. From the minimum possible radar cross-section (-30 dBsm) and the maximum range (43 m) of the radar, we estimate the minimum detectable signal of the radar to be -100 dBm from (2.8). We define the minimum signal-to-noise-ratio (SNR) of the radar receiver to be the ratio between the minimum detectable signal of the radar and the average noise power (N_p). In our study we vary the SNR from -30 to $+5$ dB. We consider a scenario where both a car and a pedestrian move simultaneously before the radar following the trajectories shown in Fig. 4.1(d) and (f), respectively. The received radar signal is therefore the superposition of the scattered signals from the two targets along with noise. In order to study the detection performance of the radar, we consider the radar range-time results ($\chi_{RT}[m, r]$) where m denotes the CPI and r denotes the discrete range bin. We multiply the signal at every bin with the quadratic power of the corresponding range. This step is crucial while detecting multiple targets of differing

cross-sections because it removes the dependency of signal strength on the distance of the target from the radar. The extended targets are spread across multiple range bins and the radar cross-section of a target (car or pedestrian) at each CPI is obtained by the *coherent integration* of the range compensated signal across multiple range bins determined by the ground truth range-time plots (the rest of the range bins have noise). For instance, the radar cross-section of the car σ_{car} at every m^{th} CPI is obtained by

$$\sigma_{\text{car}}(m) = \left\| \sum_{b=1}^B \chi_{RT}[m, r_b] r_b^2 e^{+j2\frac{2\pi}{\lambda} r_b} \right\|^2 \quad (5.1)$$

where $\{r_b\}_{b=1}^B$ denotes range bins determined from the ground truth car data for that CPI.

In Fig. 5.4, we plot the histogram distribution of the noise and target returns for both SG and MG sequences, from all the CPIs, under two different SNRs: -20 and $+5$ dB. The histograms of the car and pedestrian RCS do not show significant variation for SG and MG. Hence, we show a single distribution for each of these targets. It is evident that the RCS of the car fluctuates from -10 dBsm to 30 dBsm with a mean of 10 dBsm. In case of pedestrian, the RCS is in the range -20 to $+5$ dBsm. The variation in the RCS arises from the change in aspect angle with respect to the radar. The car thus has noticeably higher RCS than the pedestrian, as expected. The noise returns are higher under poor SNR conditions. From both histograms, it follows that the noise returns for SG are higher than those for MG because noise is added to high range sidelobes in case of SG.

The empirical probability of detection (P_d) of the radar is estimated from the area under the target histograms that falls above a RCS threshold, γ (indicated by the dashed line in the Fig. 5.4). Similarly, the empirical probability of false alarms (P_{fa}) is determined from the area under the noise histograms that falls above threshold. The P_d for SG and MG are plotted as a function of γ in Fig. 5.4c. The P_d for both targets expectedly decrease as we increase the threshold. The SG and MG waveforms show similar detection results because the modification in the Golay sequences affects only the range sidelobes, not the peak signal strength. At a threshold of -15 dBsm, the detection is close to 99% and for -20 dBsm, it is 100% .

Next, we examine the P_{fa} in Fig. 5.4d for three different thresholds. With the increase in threshold, P_{fa} decreases. We do not opt for thresholds above -15 dBsm because it leads to low P_d . When the threshold is -15 dBsm, SG exhibits higher P_{fa} than MG

by approximately 2.5% for low SNRs (-20 to 0 dB). This is even more pronounced for the -20 dBsm threshold curve because the high SG range sidelobes with additive noise show up as false alarms. When the noise is very high (-30 dB), the noise peaks are above the range sidelobe levels. Hence the P_{fa} of SG and MG become similar. For moderate-to-high SNR, i.e. 0 to $+5$ dBsm, P_{fa} for SG is higher than MG for -20 dBsm threshold.

Chapter 6

Conclusion

6.1 Conclusion

We presented a USRR which employs the 512-bit Golay codes in 802.11ad link for range estimation up to 40 m with a resolution of 0.085 m. The codes in consecutive packets form Golay complementary sequences based on the PTM sequence that results in very low sidelobe levels for most automotive targets moving up to 144 km/hr. We demonstrated detection of high range resolution profiles and micro-Doppler spectrograms of common automotive targets - pedestrian, bicycle and car. Each of these targets were animated and modeled as extended targets with multiple scattering centers distributed along their body. The signatures from the targets show distinctive micro-motion features such as the rotation of the wheels and the swinging motions of the arms and legs. The detection performance of the radar shows a marked reduction in the P_{fa} for the MG when compared to SG for low and moderate SNRs.

Bibliography

- [1] K. Bengler, K. Dietmayer, B. Farber, M. Maurer, C. Stiller, and H. Winner, “Three decades of driver assistance systems: Review and future perspectives,” *IEEE Intelligent Transportation Systems Magazine*, vol. 6, no. 4, pp. 6–22, 2014.
- [2] Z. Slavik and K. V. Mishra, “Phenomenological modeling of millimeter-wave automotive radar,” in *URSI Asia-Pacific Radio Science Conference*, 2019, in press.
- [3] L. Kong, M. K. Khan, F. Wu, G. Chen, and P. Zeng, “Millimeter-wave wireless communications for IoT-cloud supported autonomous vehicles: Overview, design, and challenges,” *IEEE Communications Magazine*, vol. 55, no. 1, pp. 62–68, 2017.
- [4] K. V. Mishra, A. Zhitnikov, and Y. C. Eldar, “Spectrum sharing solution for automotive radar,” in *IEEE Vehicular Technology Conference - Spring*, 2017, pp. 1–5.
- [5] M. Gerla, E.-K. Lee, G. Pau, and U. Lee, “Internet of vehicles: From intelligent grid to autonomous cars and vehicular clouds,” in *IEEE World Forum on Internet of Things*, 2014, pp. 241–246.
- [6] C. Premebida, O. Ludwig, and U. Nunes, “LIDAR and vision-based pedestrian detection system,” *Journal of Field Robotics*, vol. 26, no. 9, pp. 696–711, 2009.
- [7] F. Xu, X. Liu, and K. Fujimura, “Pedestrian detection and tracking with night vision,” *IEEE Transactions on Intelligent Transportation Systems*, vol. 6, no. 1, pp. 63–71, 2005.
- [8] L. Li, F. Zhou, and X. Bai, “Infrared pedestrian segmentation through background likelihood and object-biased saliency,” *IEEE Transactions on Intelligent Transportation Systems*, no. 99, pp. 1–19, 2017.

- [9] K. V. Mishra, M. R. Bhavani Shankar, V. Koivunen, B. Ottersten, and S. A. Vorobyov, "Toward millimeter wave joint radar communications: A signal processing perspective," *IEEE Signal Processing Magazine*, 2019, in press.
- [10] K. V. Mishra and Y. C. Eldar, "Performance of time delay estimation in a cognitive radar," in *IEEE International Conference on Acoustics, Speech, and Signal Processing*, 2017, pp. 3141–3145.
- [11] K. V. Mishra, Y. C. Eldar, E. Shoshan, M. Namer, and M. Meltsin, "A cognitive sub-Nyquist MIMO radar prototype," *arXiv preprint arXiv:1807.09126*, 2018.
- [12] J. Harding, G. Powell, R. Yoon, J. Fikentscher, C. Doyle, D. Sade, M. Lukuc, J. Simons, and J. Wang, "Vehicle-to-vehicle communications: Readiness of V2V technology for application," National Highway Traffic Safety Administration, Tech. Rep. DOT HS 812 014, 2014.
- [13] S. H. Dokhanchi, M. R. Bhavani Shankar, K. V. Mishra, and B. Ottersten, "A mmWave automotive joint radar-communication system," *IEEE Transactions on Aerospace and Electronic Systems*, 2019, in press.
- [14] A. Ayyar and K. V. Mishra, "Robust communications-centric coexistence for turbo-coded OFDM with non-traditional radar interference models," in *IEEE Radar Conf.*, 2019, in press.
- [15] P. Kumari, N. González-Prelcic, and R. W. Heath Jr., "Investigating the IEEE 802.11ad standard for millimeter wave automotive radar," in *IEEE Vehicular Technology Conference - Spring*, 2015, pp. 1–5.
- [16] E. Grossi, M. Lops, L. Venturino, and A. Zappone, "Opportunistic radar in IEEE 802.11ad networks," *IEEE Transactions on Signal Processing*, vol. 66, no. 9, pp. 2441–2454, 2018.
- [17] G. R. Muns, K. V. Mishra, C. B. Guerra, Y. C. Eldar, and K. R. Chowdhury, "Beam alignment and tracking for autonomous vehicular communication using IEEE 802.11ad-based radar," in *IEEE Infocom Workshops - Hot Topics in Social and Mobile Connected Smart Objects*, 2019, in press.
- [18] M. A. Richards, *Fundamentals of radar signal processing*. McGraw-Hill, 2005.
- [19] F. G. Jansen, "Automotive radar sensor for ultra short range applications," in *International Radar Symposium*, 2017, pp. 1–6.

- [20] V. C. Chen, "Analysis of radar micro-Doppler with time-frequency transform," in *IEEE Workshop on Statistical Signal and Array Processing*, 2000, pp. 463–466.
- [21] V. C. Chen, F. Li, S.-S. Ho, and H. Wechsler, "Micro-Doppler effect in radar: Phenomenon, model, and simulation study," *IEEE Transactions on Aerospace and Electronic Systems*, vol. 42, no. 1, pp. 2–21, 2006.
- [22] S. S. Ram, C. Christianson, and H. Ling, "Simulation of high range-resolution profiles of humans behind walls," in *IEEE Radar Conference*, 2009, pp. 1–4.
- [23] S. Björklund, H. Petersson, A. Nezirovic, M. B. Guldogan, and F. Gustafsson, "Millimeter-wave radar micro-Doppler signatures of human motion," in *IEEE International Radar Symposium*, 2011, pp. 167–174.
- [24] K. V. Mishra and Y. C. Eldar, "Sub-Nyquist channel estimation over IEEE 802.11ad link," in *IEEE International Conference on Sampling Theory and Applications*, 2017, pp. 355–359.
- [25] K. V. Mishra, V. Chandrasekar, C. Nguyen, and M. Vega, "The signal processor system for the NASA Dual-frequency Dual-polarized Doppler Radar," in *IEEE International Geoscience and Remote Sensing Symposium*, 2012, pp. 4774–4777.
- [26] K. V. Mishra, "Frequency diversity wideband digital receiver and signal processor for solid-state dual-polarimetric weather radars," Master's thesis, Colorado State University, 2012.
- [27] A. Pezeshki, A. R. Calderbank, W. Moran, and S. D. Howard, "Doppler resilient Golay complementary waveforms," *IEEE Transactions on Information Theory*, vol. 54, no. 9, pp. 4254–4266, 2008.
- [28] N. Levanon and E. Mozeson, *Radar signals*. John Wiley & Sons, 2004.
- [29] R. Sivaswamy, "Self-clutter cancellation and ambiguity properties of subcomplementary sequences," *IEEE Transactions on Aerospace and Electronic Systems*, no. 2, pp. 163–181, 1982.
- [30] J. P. Allouche and J. Shallit, "The ubiquitous Prouhet-Thue-Morse sequence," in *Sequences and Their Applications*, T. H. C. Ding and H. Niederreiter, Eds. Springer-Verlag, 1999.

- [31] G. Duggal, S. S. Ram, and K. V. Mishra, “Micro-Doppler and micro-range detection via Doppler-resilient 802.11ad-based vehicle-to-pedestrian radar,” in *IEEE Radar Conference*, 2019, in press.
- [32] *Wireless LAN Medium Access Control (MAC) and Physical Layer (PHY) Specifications Amendment 3: Enhancements for Very High Throughput in the 60 GHz Band*, 2012, IEEE Std. 802.11ad.
- [33] A. F. Molisch, *Wireless communications*. John Wiley & Sons, 2012.
- [34] S. S. Ram and H. Ling, “Simulation of human microDopplers using computer animation data,” in *IEEE Radar Conference*, 2008, pp. 1–6.
- [35] E. Coumans and Y. Bai, “PyBullet quickstart guide,” <https://pythonhosted.org/pybullet/>, 2017-2018.
- [36] E. Kokkevis, D. Metaxas, and N. I. Badler, “User-controlled physics-based animation for articulated figures,” in *IEEE Computer Animation*, 1996, pp. 16–26.
- [37] S. S. Ram, C. Christianson, Y. Kim, and H. Ling, “Simulation and analysis of human micro-Dopplers in through-wall environments,” *IEEE Transactions on Geoscience and Remote Sensing*, vol. 48, no. 4, pp. 2015–2023, 2010.
- [38] G. T. Ruck, D. E. Barrick, W. D. Stuart, and C. K. Krichbaum, *Radar cross section handbook*. Plenum press New York, 1970, vol. 1.